Available online at www.sciencedirect.com

SciVerse ScienceDirect

Ceramics International 38 (2012) 2087–2094

CERAMICS
INTERNATIONAL

www.elsevier.com/locate/ceramint

Influence of CeO_2 addition on crystal growth behavior of CeO_2–Y_2O_3–ZrO_2 solid solution

Chunjie Wang [a,b], Yue Wang [a], Wenzhi Huang [a,b], Binglin Zou [a], Zuhair Subhani Khan [a], Yu Zhao [a,b], Jili Yang [a,b], Xueqiang Cao [a,*]

[a] *State Key Laboratory of Rare Earth Resources Utilization, Changchun Institute of Applied Chemistry, Chinese Academy of Sciences, Changchun 130022, China*

[b] *Graduate School of Chinese Academy of Sciences, Beijing 100039, China*

Received 8 August 2011; received in revised form 3 October 2011; accepted 16 October 2011
Available online 23 October 2011

Abstract

Nanopowders with cubic fluorite-type structure as well as uniform distribution in particle size were synthesized by hydrothermal method in the ternary oxide zirconia–yttria–ceria system with ceria content of 0–25 mol%. X-ray diffraction (XRD), thermogravimetric analysis/differential scanning calorimeter (TG/DSC), Fourier transform infrared spectroscopy (FT-IR), Raman spectroscopy (Raman), specific surface area (S_{BET}) and high resolution transmission electron microscopy (HRTEM) were applied to characterize the structure, thermal decomposition, morphological characteristic and crystal growth of the produced powders. Qualitative analyses indicate that the as-synthesized nanoparticles are single-phase crystallites with an average particle size of 4–9 nm. The specific surface area, lattice parameter and microstrain are closely related to Ce^{4+} concentration. Moreover, activation energy of crystal growth is significantly dependent on the dopant (CeO_2) concentration. It firstly increased and then decreased with increasing dopant concentration, and the maximum value was observed at the dopant concentration of 5 mol%.

Keywords: A. Doping; B. Nanomaterials; C. Thermal properties; D. Rare earth compounds

1. Introduction

Yttria stabilized zirconia (YSZ) has been successfully used in many areas of science and technology, such as solid oxide fuel cells (SOFC), oxygen sensors, thermal barrier coatings, etc. [1–3]. Moreover, it is also considered as an attractive matrix for nuclear applications due to its high radiation stability, high melting point, small neutron capture cross section and high leaching resistance. For the reasons mentioned above, YSZ is generally used to form solid solution in a wide range of solubility with some actinide compounds including UO_2, ThO_2 and PuO_2. As revealed in several investigations, most studies related to inert matrices were initially performed by synthesizing an inactive material involving in the actinide incorporation of cerium or other lanthanides [4–7].

During the past few years, the ternary system ZrO_2–Y_2O_3–CeO_2 has been studied in detail. For example, Naito et al. [8] devoted their works on the oxygen transport properties of ZrO_2–CeO_2–Y_2O_3 system. Duh and Lee [9] reported that the structural stability of materials based on ZrO_2–Y_2O_3 could be enhanced by the addition of CeO_2 (5–20 mol%). Bukaemskiy et al. [10] investigated the thermal and crystallization behaviors of CeO_2–8YSZ (8 mol% Yttria stabilized zirconia) with CeO_2 concentration ranging from 0 to 100 mol%. However, to the best of our knowledge, evidences for crystallization peculiarities and quantitative information on the evolution of crystal growth in the ZrO_2–Y_2O_3–CeO_2 system have not yet been reported in literature. It is well known that there are two competitive processes namely crystallization and sintering during heat treatment [11,12]. Crystallization makes densification more difficult, so it is necessary to investigate the crystal growth behavior. In addition, the influences of annealing temperature and concentration of CeO_2 on the properties of final ceramic materials have a great scientific and practical interest, especially for nuclear applications. In this work, the

---

* Corresponding author. Tel.: +86 431 85262285; fax: +86 431 85262285.
E-mail address: xcao@ciac.jl.cn (X. Cao).

0272-8842/$36.00. Crown Copyright © 2011 Published by Elsevier Ltd and Techna Group S.r.l. All rights reserved.
doi:10.1016/j.ceramint.2011.10.046

crystal growth behavior of ZrO_2–Y_2O_3–CeO_2 has been studied, and the effect of Ce^{4+} content on the activation energy of crystal growth is also discussed.

Moreover, nano-sized materials exhibit superior mechanical, electrical and thermal properties compared to the conventional coarse-grained counterparts. To improve the physicochemical properties of materials, it is essential to make insight into the characteristics at the nanolevel. Recently, hydrothermal method is considered as one of the most promising techniques to fabricate various nanopowders. The main advantages are related to the homogeneous nucleation processes and the fine grain size due to the elimination of the calcination procedure [13].

In this paper, CeO_2–8YSZ nanopowders with CeO_2 molar fraction from 0 to 25 mol% were synthesized via hydrothermal method. Cerium is considered as a surrogate for the actinides. The effects of doping concentration on the physicochemical properties of the produced powders were studied. The activation energies of crystal growth (Q) for the samples were also investigated.

2. Experimental

CeO_2–8YSZ nanocrystalline powders with different CeO_2 contents (0, 5, 10, 15, 20 and 25 mol%) were synthesized via the hydrothermal method. CeO_2, Y_2O_3 (99.9%, Guangdong Chenghai Sanxing Chemicals Ltd.) and $ZrOCl_2 \cdot 8H_2O$ (99%, Shanghai Chemicals Ltd.) were used as starting materials. Appropriate amounts of CeO_2 and Y_2O_3 were firstly dissolved in concentrated nitric acid and then mixed with a stoichiometric $ZrOCl_2 \cdot 8H_2O$ aqueous solution to give a final molar concentration of 0.1 M. The pH value of the solution was adjusted to 7 by adding sodium hydroxide solution (2 M). After homogenization, a certain amount of polyethyleneglycol (2 wt%, Shanghai Chemicals Ltd.) was added as a dispersant. CeO_2–8YSZ nanopowders were finally obtained by hydrothermal treatment of the suspension in a Teflon autoclave at 200 °C for 24 h. In order to reduce agglomeration and remove the soluble chlorides, the precipitates were filtered and washed with distilled water and ethanol for several times, and then dried at 70 °C for 12 h.

For crystal growth investigations, some powders were calcined at different temperatures. A typical regime involved a heating rate of 5 °C min^{-1} to the selected temperature and then cooling down at 5 °C min^{-1} after soaking for 5 h.

The crystalline phases of $nCeO_2$–8YSZ nanocrystalline powders calcined at different temperatures were identified by powder X-ray diffraction (XRD, Bruker D8 Focus powder X-ray diffractometer) using Cu Kα radiation (λ = 1.5406 Å) with a scanning rate of 0.4 ° min^{-1}. The operation voltage and current were maintained at 40 kV and 40 mA, respectively.

Fourier transmission infrared spectra (400–4000 cm^{-1}, Bruker Vertex 70 FTIR) of calcined powders were measured with KBr as the solid solvent. FT–Raman spectrum was recorded by a Thermo Nicolet 960 instrument with an excitation wavelength of 1064 nm, and the measured wave

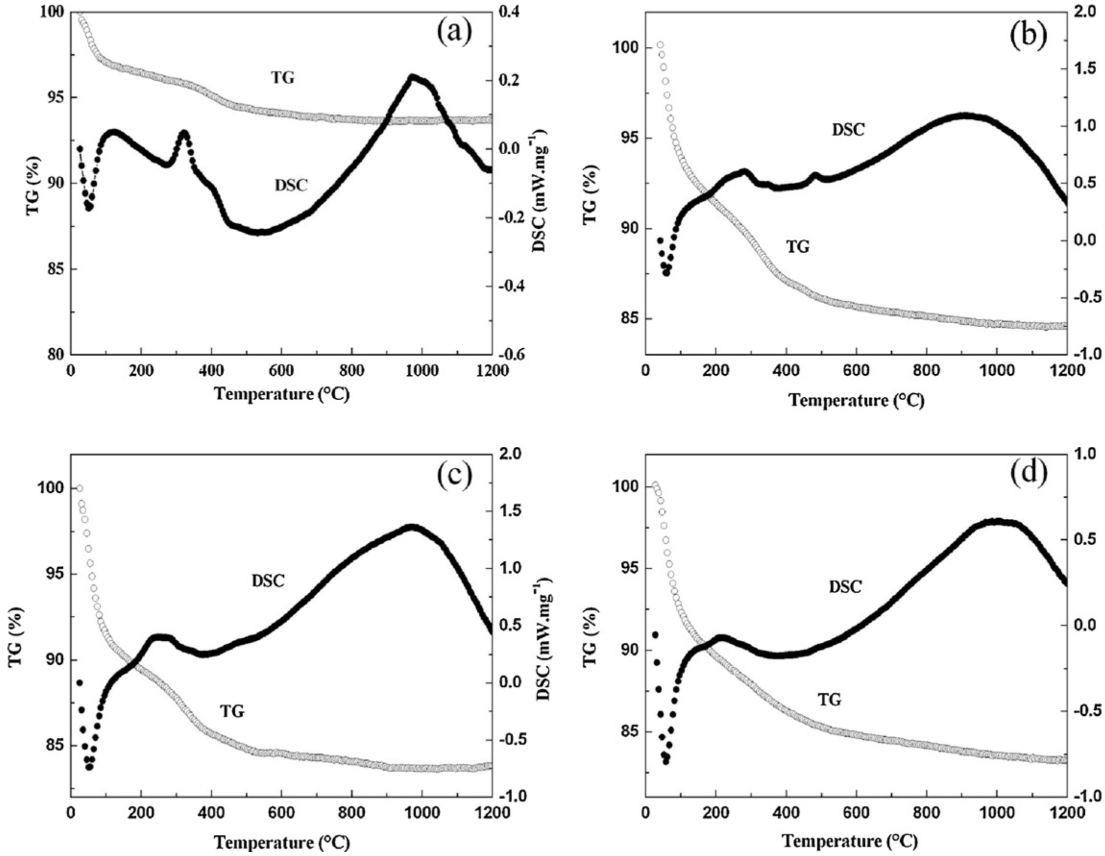

Fig. 1. TG and DSC curves of 8YSZ (a), $5CeO_2$–8YSZ (b), $15CeO_2$–8YSZ (c) and $25CeO_2$–8YSZ (d) powders.

number range is from 100 to 900 cm^{-1}. TEM and HRTEM were recorded on a JEOL-JEM-2010 operating at 200 kV (JEOL, Japan). Samples for TEM observation were prepared by dropping a diluted suspension of the powders onto a standard carbon-coated Formvar film (20–30 nm). The thermal behavior of the dried powder was studied in the temperature range of 300–1473 K using thermogravimetric analysis and differential scanning calorimeter (TG/DSC) in air with a heating rate of 10 K min^{-1} using a Netzsch STA 449 C Jupiter apparatus. The specific surface area (S_{BET}) was determined by applying Brunauer–Emmet–Teller (BET) equation [13,14] with a Micromeritics ASAP2020 instrument.

3. Results and discussion

The thermal behaviors of $nCeO_2$–8YSZ powders were investigated by TG/DSC in air atmosphere. Fig. 1 shows the TG/DSC curves of $nCeO_2$–8YSZ ($n = 0$, 5, 15, and 25) powders. In the case of TG curves, for $5CeO_2$–8YSZ (Fig. 1(b)), a significant mass loss (about 15.6%) was revealed during heating from 25 to 650 °C. The similar result could be observed in $15CeO_2$–8YSZ and $25CeO_2$–8YSZ, as displayed in Fig. 1(c) and (d). However, in the case of 8YSZ (Fig. 1(a)), only 6.9% of mass loss was observed. Furthermore, from the TG curve of 8YSZ, the weight loss could hardly be observed at temperatures above 500 °C indicating a complete decomposition of organic substances [15], and this temperature was lower than that (about 600 °C) of $nCeO_2$–8YSZ ($n = 5$, 15, and 25). In our study, the mass loss mainly derived from the desorption of physically absorbed water and the decomposition of nitrates and organic substances.

In the case of DSC curves, an endothermic process with peak temperature at about 60–80 accompanying with a mass loss of 2–3% for 8YSZ and 7–8% for $nCeO_2$–8YSZ ($n = 5$, 15, and 25) can be observed, respectively. This endothermic peak can be attributed to the loss of lattice water [16], which becomes more remarkable in the doped 8YSZ. In addition, the thermal process observed on the DSC curves at 200–600 °C might have been resulted from the decomposition of nitrates and organic substances [17–19]. The broad peak in the range of 650–1200 °C indicated that the reaction is of exothermic type [20].

Based on the TG/DSC results, some powders were calcined at different temperatures and further analyzed by XRD. The corresponding results are shown in Fig. 2. The diffraction peaks in the XRD patterns reveal that the materials crystallize in a cubic fluorite-type structure (JCPDS-file No. 30-1468). As shown in Fig. 2(a), for 8YSZ, the peaks at around $2\theta = 29.9°$, 34.6°, 49.8° and 59.1° are assigned to the (1 1 1), (2 0 0), (2 2 0) and (3 1 1) reflections. The decrease in the FWHM of peaks with increasing calcination temperature indicates an increase in crystallite size as the calcination temperature increased. For comparison, the $5CeO_2$–8YSZ and $25CeO_2$–8YSZ were also investigated. As shown in Fig. 2(b) and (c), the diffraction peak widths of $nCeO_2$–8YSZ are wider than that of 8YSZ, indicating that the grain size of the former is smaller than that of 8YSZ. Moreover, the positions of the characteristic peaks are shifted to lower angle with the increasing Ce^{4+} content, which implies that doping Ce^{4+} results in the expansion of 8YSZ cell volume. Besides, no other obvious differences can be found among those curves. No peaks corresponding to the individual oxides (CeO_2, Y_2O_3, etc.) were observed throughout the heating

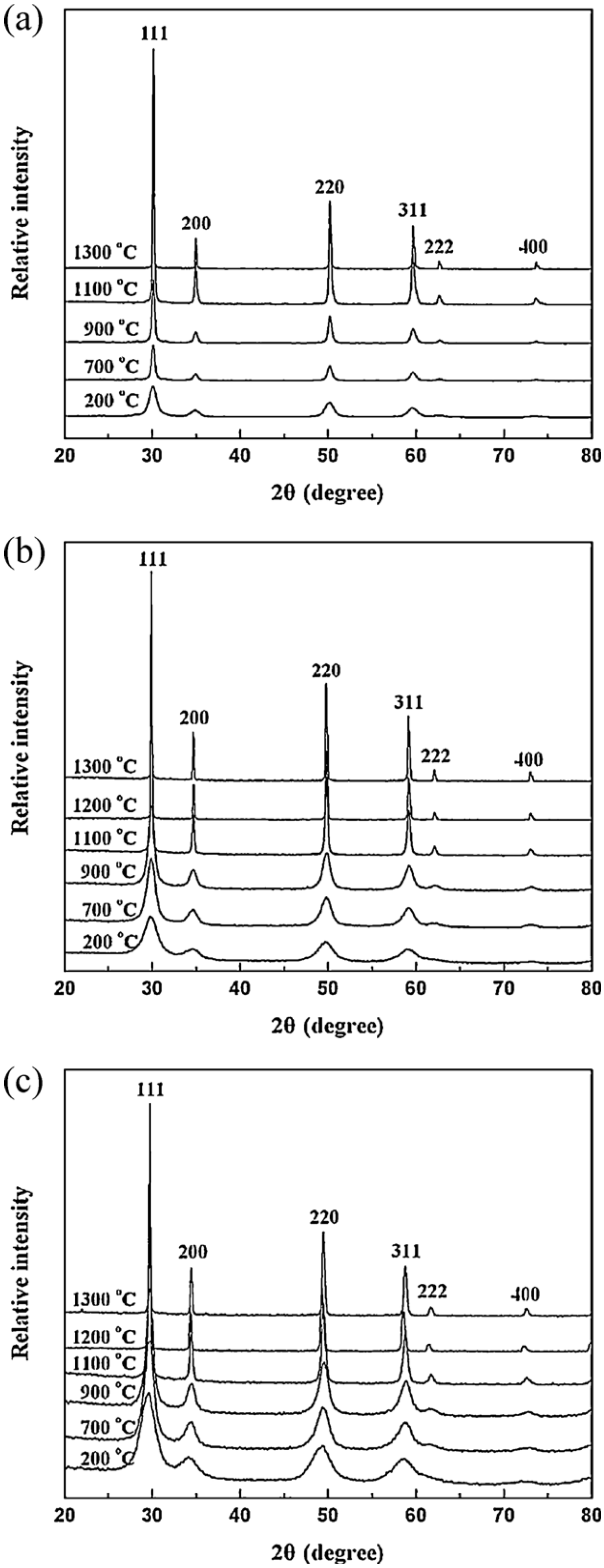

Fig. 2. X-ray diffraction patterns of 8YSZ (a), $5CeO_2$–8YSZ (b) and $25CeO_2$–8YSZ (c) powders calcined at different temperatures.

process, which suggests that CeO_2 and Y_2O_3 have completely dissolved into ZrO_2 crystal.

Because the ionic radius of Ce^{4+} (0.97 Å) is larger than that of Zr^{4+} (0.84 Å), doping with Ce^{4+} would result in the expansion of the cell volume. Fig. 3 shows the relationship between the lattice parameters calculated from XRD patterns and the CeO_2 content. The linear relationship shown in Fig. 3 illuminates that 8YSZ and CeO_2 nearly form an ideal solid solution, which is in agreement with that reported by Sammes et al. [21]. It is known that CeO_2 can react with 8YSZ to form a homogeneous solid solution; therefore, the addition of CeO_2 would result in the increase of lattice parameters following the Vegard's Law [22,23]. Bukaemskiy et al. attributed this phenomenon to the doping crystallization mechanism that the 8YSZ matrix is mainly crystallized followed by the "embedding" of CeO_2 into 8YSZ matrix [24]. The XRD results reveal that all samples are single phase, and the continuous increase in the lattice parameter with increasing CeO_2 addition demonstrates that Ce^{4+} can well incorporate into the 8YSZ lattice even at higher concentration. The specific surface areas (S_{BET}) of the as-prepared $nCeO_2$–8YSZ (n = 0–25 mol%) are also shown in Fig. 3. It can be seen that doping has a significant effect on the S_{BET}. For 8YSZ, the S_{BET} is 145.92 $m^2\ g^{-1}$. When doped with 5 mol% Ce^{4+}, the S_{BET} significantly increases to 207.87 $m^2\ g^{-1}$. With further increasing the doping percentage of Ce^{4+}, the S_{BET} increased smoothly. It is well known that for nanomaterials, the specific surface area is closely related to the grain size. More regarding it will be discussed later.

Fig. 4 compares the FT-IR spectra of 8YSZ, $5CeO_2$–8YSZ and $25CeO_2$–8YSZ powders calcined at different temperatures in the wave number of 400–4000 cm^{-1}. As shown in Fig. 4, several characteristic absorption bands can be observed at about 1384–1398, 1625–1631 and 3393–3421 cm^{-1}. The band at 1384–1398 cm^{-1} is assigned to the characteristic band of nitrate vibrations [25,26]. The detection of intense band centered at approximately 3400 cm^{-1} is an evidence of water molecules contained in the particles. The band located at 1625–1631 cm^{-1} represents another vibration of water molecules. The two bands indicate that the formation of final structure

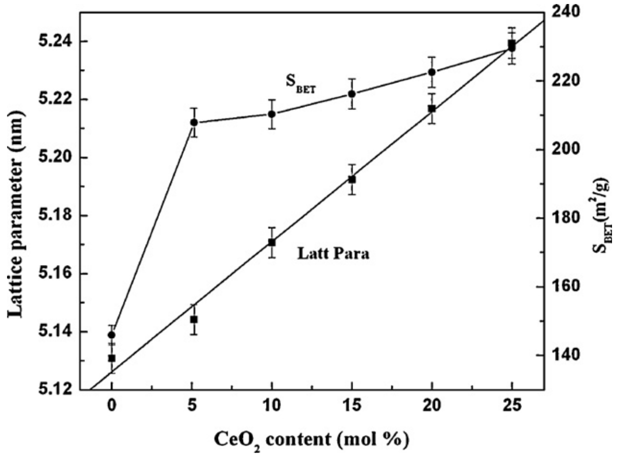

Fig. 3. Lattice constants and specific surface areas of the as-prepared $nCeO_2$–8YSZ as a function of CeO_2 content.

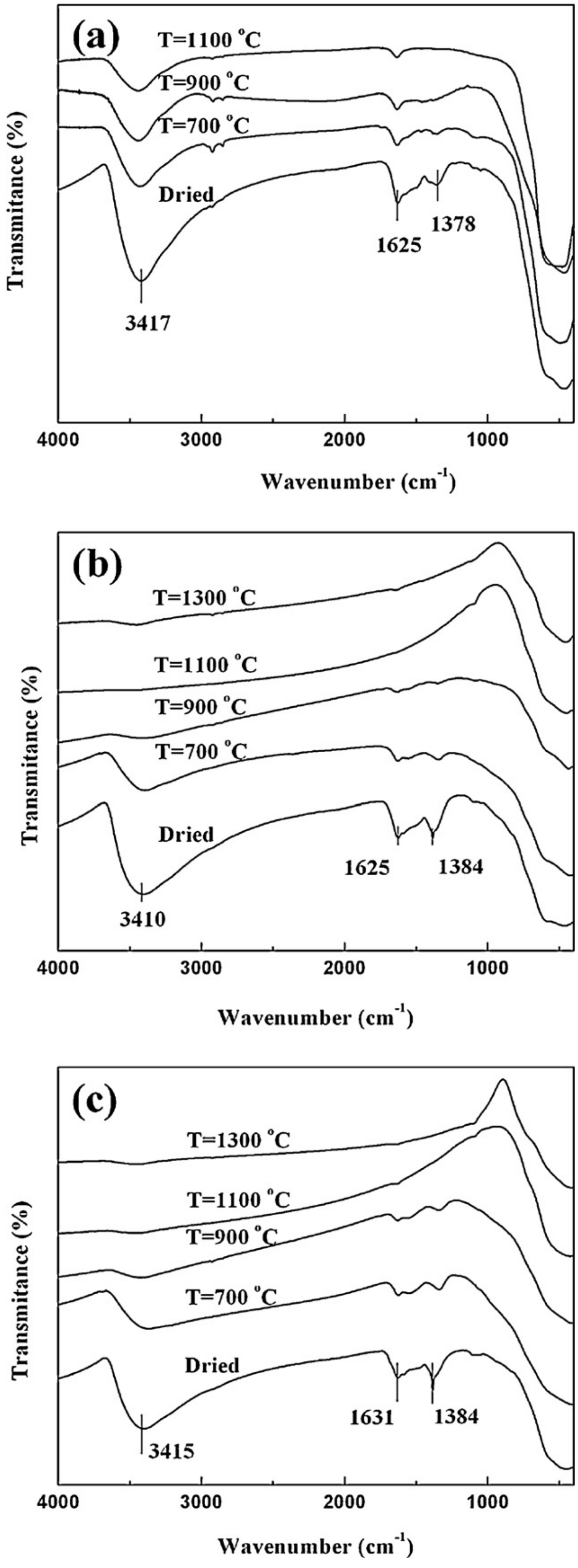

Fig. 4. Infrared spectra of 8YSZ (a), $5CeO_2$–8YSZ (b) and $25CeO_2$–8YSZ (c) powders calcined for 5 h at different temperatures.

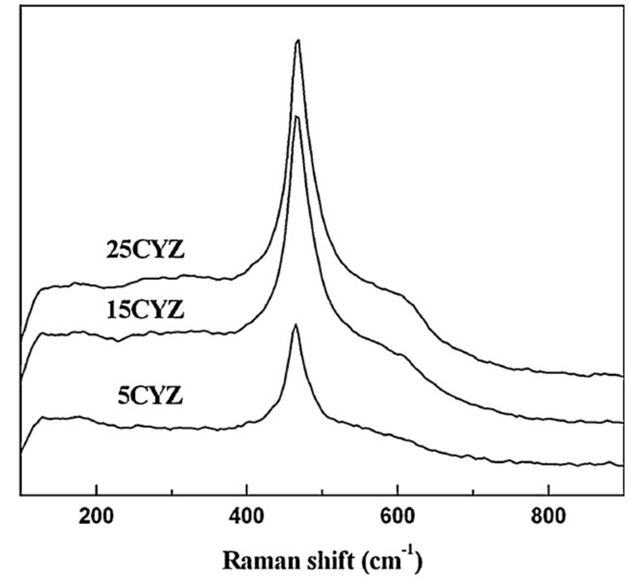

Fig. 5. FT–Raman spectra of nCeO$_2$–8YSZ ($n = 5, 15, 25$) calcined at different temperatures.

contains O–H bands [27]. These bands vanished slowly with the increasing calcination temperature.

The Raman spectra of nCeO$_2$–8YSZ ($n = 5, 15, 25$) powders calcined at 600 °C for 5 h are shown in Fig. 5. Careful investigation of the spectra revealed a detailed structure of the cubic phase. As shown in Fig. 5, the band at 465 cm^{-1} can be attributed to the F_{2g} vibration mode of cubic fluorite structure [28,29] and its intensity increases with the doping concentration increasing. This is in agreement with the XRD results. Particularly, it can be seen that a small shoulder at about 600 cm^{-1} appears with increasing Ce-concentration. Taniguchi et al. have primarily explained that this band corresponds to the second-order Raman mode attributes of O^{2-} vacancies formed by a trivalent dopant [30].

Fig. 6 shows the TEM micrographs for the as-prepared nCeO$_2$–8YSZ ($n = 0, 5, 15$, and 25) nanocrystal obtained from autoclave. As shown in Fig. 6, all samples have a good dispersion and the average particle sizes of 8YSZ, 5CeO$_2$–8YSZ, 15CeO$_2$–8YSZ and 25CeO$_2$–8YSZ are 8.72, 5.75, 4.39 and 4.16 nm, respectively. The determined mean size is the averaged value of ten particles selected randomly in the figure. It is well known that densification and grain growth is closely bound up with cation diffusion, and the retardation effects of dopants were mainly explained by the following two aspects [31,32]: (1) the solute drag mechanism. Based on the ‘‘space charge’’ model, dopants of a negative effective charge relative to Zr^{4+} would enrich at the grain-boundary region forming a space charge layer, pining grain-boundary migration and thus resulting in an effective retardation of grain growth; (2) defect clustering and lattice distortion mechanism. The difference in the ionic sizes could cause local distortion (strain energy) in the crystal structure. The presence of large numbers of defects on the grain surface, which mainly comes from nanometer small size effect, makes the surface energy changed drastically. The

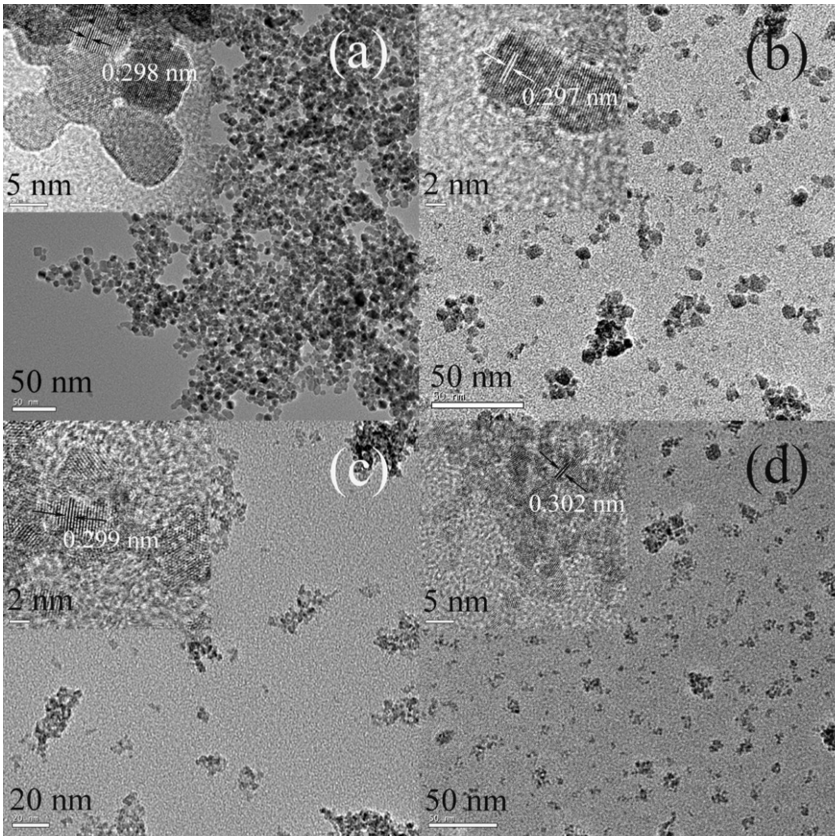

Fig. 6. TEM and HRTEM images of the as-prepared 8YSZ (a), 5CeO$_2$–8YSZ (b), 15CeO$_2$–8YSZ (c) and 25CeO$_2$–8YSZ (d).

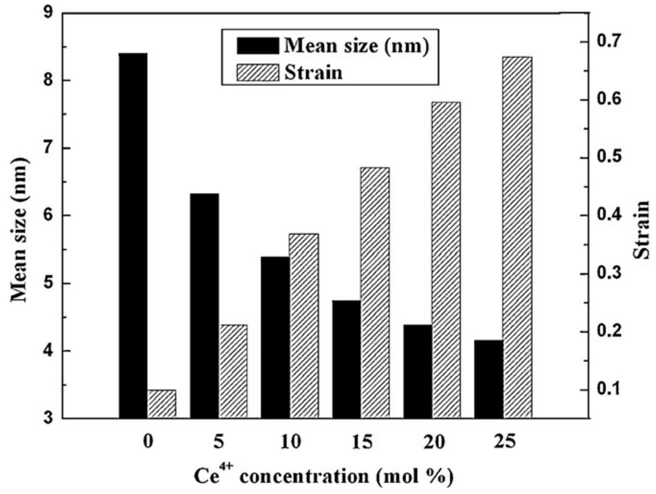

Fig. 7. The mean size and microstrain of the as-prepared nCeO_2–8YSZ (n = 0, 5, 10, 15, 20, and 25).

combined effects of strain energy and defect aggregation may slow down the mobility of cations, leading to slower grain coarsening [33]. Considering the influence of microstrain on the peak broadening, the Scherrer equation is not appropriate. In this case, contributions from both size and microstrain should be considered. If the Scherrer equation is modified in such a way, the following relation is obtained [34,35]:

$$\beta\cos\theta = \frac{k\lambda}{L} + 4\varepsilon\sin\theta \tag{1}$$

where L is the mean size, ε is the microstrain, λ is the wavelength of X-ray radiation, θ is the diffraction angle, k is a constant (0.89) and β is the corrected full-width half maximum (FWHM). From the analysis of the slope, the microstrain (ε) is determined, and from the intercept of the line with the y-axis, the mean size (L) is obtained. The mean size and microstrain of nCeO_2–8YSZ (n = 0–25) are displayed in Fig. 7. It can be noted that, the mean size decreased from 8.41 to 3.96 nm and the microstrain increased from 0.0988 to 0.6741 with the Ce^{4+} concentration increasing from 0 to 25 mol%. The size data are in agreement with the results obtained by TEM. Higher concentrations of doping would create larger microstrain, bringing about lower growth rate to form nanoparticles with smaller size. A similar result was obtained by Weidenthaler [34], which indicated that the microstrain increased with the decrease of mean size. Also, as mentioned above, the specific surface area is closely tied to the grain size. The smaller the grain size is, the larger the S_{BET} would be. The grain size of as-prepared samples was calculated according to Eq. (1) (as shown in Fig. 7). The grain size of the products decreased with increasing the doping concentration, as has been mentioned above; as a result, the specific surface area of 25CeO_2–8YSZ is the largest among these samples.

HRTEM was also employed to obtain information about the internal structure of the produced nCeO_2–8YSZ nanocrystallites (inset in Fig. 6). The 8YSZ clearly exhibits the resolved lattice fringe with an interplanar spacing of 0.298 nm (Fig. 6(a)). With increasing the doping concentration, interplanar spacing of (1 1 1) plane increases from 0.297 (5CeO_2–8YSZ) to 0.299 (15CeO_2–8YSZ) and to 0.302 nm (25CeO_2–8YSZ). This suggests that nCeO_2–8YSZ can form high-quality solid solution.

Fig. 8(a) illustrates the relationship between the calcination temperature and the average size of nCeO_2–8YSZ (n = 0–25 mol%). As shown in Fig. 8(a), with the temperature increasing from 700 to 1300 °C, the average size of 8YSZ changed from 9.73 to 89.98 nm. It could be contributed to the fact that the rise in reaction temperature increases the crystal growth rate. On the other hand, the average crystallite sizes of nCeO_2–8YSZ (n = 5–25 mol%) increase from 7.82, 7.01, 6.22, 6.01 and 5.34 nm to 82.75, 75.01, 62.97, 50.29 and 35.08 nm, respectively.

In order to further investigate the crystal growth behavior of nCeO_2–8YSZ (n = 0–25 mol%), the activation energies of crystal growth (Q) with various compositions were studied. The logarithms of average crystallite size versus the reciprocal of calcination temperature are plotted in Fig. 8(b) by linear fitting, assuming that the crystal growth of nCeO_2–8YSZ is a thermally

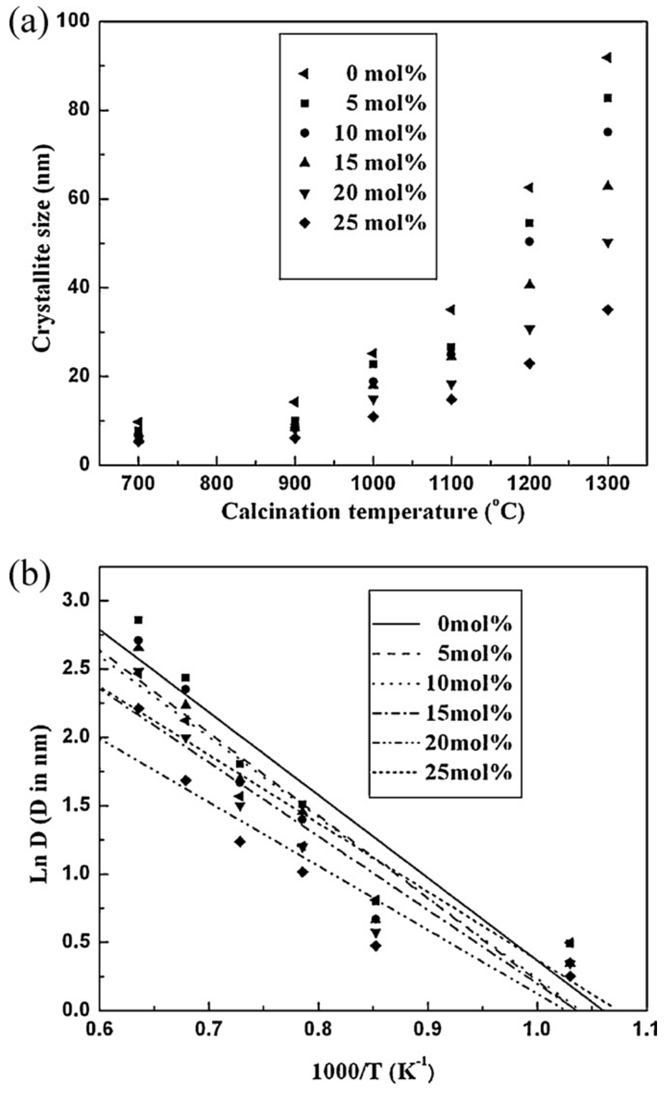

Fig. 8. Effects of calcination temperature on the nanocrystallite sizes of nCeO_2–8YSZ (n = 0–25 mol%) (a) and plots of ln(D) against 1000/T (b).

activated process. According to the following formula [36]:

$$D_t = D_0 \times e^{(-Q/RT)} \quad (2)$$

where D_0 and D_t are the initial and final average sizes (nm), R denotes the ideal gas constant (kJ K^{-1} mol^{-1}), and T is the calcination temperature (K). The effective activation energy of crystal growth can be obtained by calculating the plot slope of ln(D) versus 1000/T (Fig. 8(b)). For 8YSZ, the obtained activation energy is 66.27 ± 0.09 kJ mol^{-1}. Doping can lead to an interesting change on activation energy which first increased and then decreased with the increasing dopant concentration. From Fig. 8(b), it can be observed that the activation energy showed a slight increase to 69.09 ± 0.08 kJ mol^{-1} for $5CeO_2$–8YSZ. Further increasing the doping concentration would result in the decrease of activation energy (52.88 ± 0.12 kJ mol^{-1} for $25CeO_2$–8YSZ). Unfortunately, data on activation energy for CeO_2 doping 8YSZ crystal growth from hydrothermal synthesis is scarce in the literature.

During the calcination treatment of such a free-standing powder at high temperature, the increase in particle size is mainly resulted from the elimination of boundaries between the nanocrystallites within the hard aggregates [37]. However, the nature of coalescence phenomenon is still unclear, especially for nanomaterials. Existing models explain it as a result of the uneven distribution of the pinning admixtures, which result in remarkable difference in the mobility of free and solute dragged crystallite boundaries [38]. However, from our data it can be seen that doping with Ce^{4+} (from 5% to 25%), in comparison with 8YSZ, first promotes crystal growth and then restrains it. The fact that fast growth is induced by small doping quantity ($5CeO_2$–8YSZ) indicates that introduced Ce^{4+} do not cause the crystallite boundary retardation. With Ce^{4+} concentration increasing, the crystal growth rate becomes slow. This fact indicates that crystallite boundary retardation becomes greater when larger ratio Ce^{4+} is introduced in 8YSZ. This result is similar with Sikong's result [39], who reported that addition of 1–5 mol% SnO_2 with fixed TiO_2 content rendered a slight effect on the growth of anatase crystallite. However, 10 mol% or more SnO_2 doping tended to hinder the TiO_2 growth. Bonnet et al. also found that small addition of second phase (0.01 mol% of copper oxide) drastically increases densification of microcrystalline SnO_2 [40], whereas the higher doping result was not discussed.

Majority of the theories explain crystal growth as a result of thermally induced diffusion of mobile species in the lattice [41]. In contrast, for $5CeO_2$–8YSZ, not only Y_2O_3 but also CeO_2 were incorporated into the zirconia matrix. The lower activation energy for grain growth is attributed to the presence of a large concentration of oxygen vacancies existed in YSZ nanocrystalline [42]. However, for $nCeO_2$–8YSZ (n = 10–25), the same cubic (space group $Fm-3m$) structure of crystallite for both ZrO_2 and CeO_2 could result in a random distribution of Zr and Ce atoms on the cationic positions [43]. Therefore, introduction of Ce^{4+} could bring about some substitutional defects in zirconia lattice [44]. The oxygen vacancy generated in 8YSZ tends to be associated with Ce^{4+} and Zr^{4+} cations. The reduced oxygen vacancy by introduction of Ce^{4+} in 8YSZ can lead to the high activation energy in $5CeO_2$–8YSZ. However, increasing Ce^{4+} concentration inserted into 8YSZ network could decrease the activation energy for $nCeO_2$–8YSZ (n = 10–25). This phenomenon may result from the fact that the oxygen vacancies existed in 8YSZ may combine with cations when the large amount of Ce^{4+} was intruded in 8YSZ. In this case, the substitutional defects play a significant role on crystal growth.

4. Conclusions

The conclusions of this study are summarized as follows:

(1) With the doping percentage increasing from 5 to 25 mol%, only cubic fluorite-type structure phase can be detected in samples throughout the calcination temperature range. No phase transition occurred during the whole calcination temperature from 700 to 1300 °C.
(2) The specific surface areas of samples increased with increasing doping concentration which changes from 145.92 to 229.52 m^2 g^{-1}.
(3) The products are monodispersed particles with average size in the range of 4–9 nm, which decreased with the increasing Ce^{4+} concentration. The microstrain and the lattice parameter are also closely related to the doping concentration.
(4) CeO_2 doping results in the change of activation energy. With the doping percentage increasing, the activation energy increased first and then decreased, and the maximum value was observed at the dopant concentration of 5 mol%.

Acknowledgments

This work was financially supported by projects of NSFC-50825204, NSFC-20921002, NSFC-51101143 and Lotus Scholars Program of Hunan.

References

[1] A.A.E. Hassan, N.H. Menzler, G. Blass, Influence of alumina dopant on the properties of yttria-stabilized zirconia for SOFC applications, J. Mater. Sci. 37 (2002) 3467–3475.
[2] J. Will, A. Mitterdorfer, C. Kleinlogel, D. Perednis, L.J. Gauckler, Fabrication of thin electrolytes for second-generation solid oxide fuel cells, Solid State Ionics 131 (2000) 79–96.
[3] A.K. Bhattacharya, P. Reinhard, W. Steurer, V. Shklover, Calcia-doped yttria-stabilized zirconia for thermal barrier coatings: synthesis and characterization, J. Mater. Sci. 46 (2011) 5709–5714.
[4] C.H. Lee, G.M. Choi, Electrical conductivity of CeO_2-doped YSZ, Solid State Ionics 135 (2000) 653–661.
[5] C. Hellwig, M. Pouchon, R. Restani, F. Ingold, G. Bart, Fabrication and microstructure characterization of inert matrix fuel based on yttria stabilized zirconia, J. Nucl. Mater. 340 (2005) 163–170.
[6] G. Ledergerber, C. Degueldre, P. Heimgartner, M.A. Pouchon, U. Kasemeyer, Inert matrix fuel for the utilization of plutonium, Prog. Nucl. Energy 38 (2001) 301–308.
[7] A. Fernandez, D. Haas, R.J.M. Konings, J. Somers, Transmutation of actinides, J. Am. Ceram. Soc. 85 (3) (2002) 694–696.
[8] H. Naito, N. Sakai, T. Otake, H. Yugami, H. Yokokawa, Oxygen transport properties in ZrO_2–CeO_2–Y_2O_3 by SIMS analysis, Solid State Ionics 135 (2000) 669–673.

[9] J.G. Duh, M.Y. Lee, Fabrication and sinterability in Y_2O_3–CeO_2–ZrO_2, J. Mater. Sci. 24 (1989) 4467–4474.

[10] A.A. Bukaemskiy, D. Barrier, G. Modolo, Physical properties of 8 mol% ceria doped yttria stabilised zirconia powder and ceramic and their behaviour during annealing and sintering, J. Eur. Ceram. Soc. 26 (2006) 1507–1515.

[11] G.W. Scherer, Sintering of sol–gel films, J. Sol–Gel Sci. Technol. 8 (1997) 353–363.

[12] P. Duran, C. Moure, J.R. Jurado, Sintering and microstructural development of ceria–gadolinia dispersed powders, J. Mater. Sci. 29 (1994) 1940–1948.

[13] W.W. Wang, J.L. Yao, Hydrothermal synthesis of SnO_2/Fe_3O_4 nanocomposites and their magnetic property, J. Phys. Chem. C 113 (2009) 3070–3075.

[14] S. Brunauer, P.H. Emmett, E. Teller, Adsorption of gases in multimolecular laters, J. Am. Chem. Soc. 60 (1938) 309–319.

[15] Z.L. Hua, X.M. Wang, P. Xiao, J.L. Shi, Solvent effect on microstructure of yttria-stabilized zirconia particles in colvothermal synthesis, J. Eur. Ceram. Soc. 26 (2006) 2257–2264.

[16] R. Sirera, M.L. Calzada, F. Carmona, B. Jiménez, Physicochemical characterisation of lead titanate solutions applied to the processing of thin films, J. Sol–Gel Sci. Technol. 2 (1994) 545–549.

[17] X. Huang, A. Zakurdaev, D.M. Wang, Microstructure and phase transformation of zirconia-based ternary oxides for thermal barrier coating applications, J. Mater. Sci. 43 (2008) 2631–2641.

[18] S. Rossignol, Y. Madier, D. Duprez, Preparation of zirconiaceria materials by soft chemistry, Catal. Today 50 (1999) 261–270.

[19] S.V. Ushakov, C.E. Brown, A. Navrotsky, Effect of La and Y on crystallization temperatures of hafnia and zirconia, J. Mater. Res. 19 (3) (2004) 693–696.

[20] P. Zhang, Energetics of cubic and monoclinic yttrium oxide polymorphs: phase transitions, surface enthalpies, and stability at the nanoscale, J. Phys. Chem. C 112 (2008) 932–938.

[21] N.M. Sammes, G.A. Tompsett, Z.H. Cai, The chemical reaction between ceria and fully stabilized zirconia, Solid State Ionics 121 (1999) 121–125.

[22] K. Kuramoto, T. Mitamuro, T. Banba, S. Muraoka, Development of ceramic waste forms for actinide-rich waste, Prog. Nucl. Energy 32 (1998) 509–516.

[23] A. Ernandez, D. Haas, R.J.M. Konings, J. Somers, Fuel/target concepts for transmutation of actinides, in: In Proceedings of the NEAP&T Exchange Meeting 2000, Madrid, 2000.

[24] A.A. Bukaemskiy, D. Barrier, G. Modolo, Thermal and crystallization behaviour of 8YSZ–CeO_2, J. Alloys Compd. 472 (2009) 286–293.

[25] S.A. Hassanzadeh-Tabrizi, M. Mazaheri, Reverse presipitation synthesis and characterization of CeO_2 nanopowder, J. Alloys Compd. 491 (2010) 499–502.

[26] S.A. Hassanzadeh-Tabrizi, E. Taheri-Nassaj, H. Sarpoolaky, Synthesis of an alumina–YAG nanopowder via sol–gel method, J. Alloys Compd. 456 (2008) 282–285.

[27] A. Gedanken, R. Reisfeld, E. Sominski, O. Palchik, Y. Koltypin, G. Panczer, M. Gaft, H. Minti, Sonochemical preparation and characterization of europium oxide doped In and coated on ZrO_2 and yttrium-stabilized zirconium (YSZ), J. Phys. Chem. B 104 (2000) 7057–7065.

[28] C.M. Phillippi, K.S. Mazdiyasni, Infrared and Raman spectra of zirconia polymorphs, J. Am. Ceram. Soc. 54 (1971) 254–258.

[29] T. Otake, H. Yugami, H. Naito, K. Kawamura, Ce^{3+} concentration in ZrO_2–CeO_2–Y_2O_3 system studied by electronic Raman scattering, Solid State Ionics 135 (2000) 663–667.

[30] T. Taniguchi, T. Watanebe, N. Sakamoto, N. Matsushita, M. Yochimura, Aqueous route to size-controlled and doped organophilic ceria nanocrstals, Cryst. Growth Des. 8 (2008) 3725–3730.

[31] J.G. Li, T. Ikegami, T. Mori, Low temperature processing of dense samarium-doped CeO_2 ceramics: sintering and grain growth behaviors, Acta Mater. 52 (2004) 2221–2228.

[32] P.L. Chen, I.W. Chen, Grain boundary mobility in Y_2O_3: defect mechanism and dopant effects, J. Am. Ceram. Soc. 79 (1996) 1801–1809.

[33] J.G. Li, Y. Wang, T. Ikegami, Densification below 1000 °C and grain growth behaviors of yttria doped ceria ceramics, Solid State Ionics 179 (2008) 951–954.

[34] C. Weidenthaler, Pitfalls in the characterization of nanoporous and nanosized matertials, Nanoscale 3 (2011) 792–810.

[35] G.E. Rush, A.V. Chadwick, I. Kosacki, H.U. Anderson, An EXAFS study of nanocrystalline yttrium stabilized cubic zirconia films and pure zirconia powders, J. Phys. Chem. B 104 (2000) 9597–9606.

[36] K. Matusita, S. Sakka, Y. Matsui, Determination of the activation energy for crystal growth by differential thermal analysis, J. Mater. Sci. 10 (1975) 961–966.

[37] P. Shen, W.H. Lee, (1 1 1)-Specific coalescence twinning and martensitic transformation of tetragonal ZrO_2 condensates, Nano Lett. 1 (2001) 707–711.

[38] S.G. Kim, W.T. Kim, Y.B. Park, Abnormal grain growth induced by boundary segregation of solute atoms, Mater. Sci. Forum 558–559 (2007) 1093–1099.

[39] L. Sikong, K. Kooptarnond, S. Niyomwas, J. Damchan, Photoactivity and hydrophilic property of SiO_2 and SnO_2 co-doped TiO_2 nano-composite thin films, J. Sci. Technol. 32 (2010) 413–418.

[40] J.P. Bonett, N. Dolet, J.M. Heintz, Low-temperature sintering of 0.99 SnO_2–0.01 CuO: influence of copper surface diffusion, J. Eur. Ceram. Soc. 16 (1996) 1163–1169.

[41] Z.Z. Fang, H. Wang, Densification and grain growth during sintering of nanosized particles, Int. Mater. Rev. 53 (2008) 326–352.

[42] S. Shukla, S. Seal, R. Vij, S. Bandyopadhyay, Reduced activation energy for grain growth in nanocrystalline yttria-stabilized zirconia, Nano Lett. 3 (2003) 397–401.

[43] M. Gateshki, M. Niederberger, A.S. Deshpande, Y. Ren, V. Petkov, Atomic-scale structure of nanocrystalline CeO_2–ZrO_2 oxides by total X-ray diffraction and pair distribution function analysis, J. Phys.: Condens. Matter 19 (2007) 156205–156216.

[44] X. Huang, D. Wang, L. Mario, M. Christian, Experimental study of the thermal conductivity of metal oxides co-doped yttria stabilized zirconia, Mater. Sci. Eng. B 149 (2008) 63–72.